We are IntechOpen,
the world's leading publisher of
Open Access books
Built by scientists, for scientists

6,900
Open access books available

185,000
International authors and editors

200M
Downloads

154
Countries delivered to

Our authors are among the

TOP 1%
most cited scientists

12.2%
Contributors from top 500 universities

BOOK CITATION INDEX
CLARIVATE ANALYTICS
INDEXED

WEB OF SCIENCE™

Selection of our books indexed in the Book Citation Index
in Web of Science™ Core Collection (BKCI)

Interested in publishing with us?
Contact book.department@intechopen.com

Numbers displayed above are based on latest data collected.
For more information visit www.intechopen.com

Chapter

An Effective Approach for Turbine Hot Component Failure Analysis

Lei-Yong Jiang and Prakash Patnaik

Abstract

One advantage of computational fluid dynamics (CFD) is its ability to reveal the physics or nature of practical engineering problems in detail, allowing engineers and scientists to develop rigorous, effective, and efficient solutions. In this chapter, an effective approach to investigate gas turbine hot component failure is demonstrated, and the mid-span cracking of nozzle guide vanes (NGVs) is used as an example. It is a two-step approach. In the first step, a 60° combustor sector with simplified NGVs and thermocouples attached is simulated; and in the second step, NGV sectors are simulated, where each NGV sector is comprised of one high-fidelity probe NGV and several dummy NGVs. The former identifies the NGV having the highest thermodynamic load and provides the inlet boundary conditions for the latter. The CFD analysis successfully identified the root causes of the NGV damage pattern and mid-span cracking, i.e., the hot streaks from the combustor and inadequate internal cooling.

Keywords: computational fluid dynamics, gas turbine, nozzle guide vane, internal air cooling, failure analysis

1. Introduction

To achieve high thrust, the first-stage nozzle guide vanes (NGVs) of a gas turbine engine are always exposed to high-temperature, high-pressure, high-dynamic load environments and are consequently recognized as one of the most failure-prone components [1]. The thermodynamic load around and inside NGVs varies significantly, which causes considerable uneven structural stresses. For reliable structural, material, and lifetime analysis, a detailed NGV thermodynamic load is deemed necessary.

Due to the harsh conditions, experimental measurements inside the engine are extremely difficult. Computational fluid dynamics (CFD) analysis is routinely used and continuously validated to calculate NGV thermodynamic loads. The heat transfer between the NGV/shrouds and hot-gas flow of a gas turbine combustor was simulated by Mazur et al. [2]. They pointed out that it was feasible to assess the NGV remaining lifetime from the predicted thermodynamic loads and stress and creep strain analyses. Nonetheless, in the paper the shroud thermal boundary conditions were not provided. The heat transfer simulation of a film-cooled linear cascade was performed and validated against the measured data by Harsqama et al. [3]. It was found that the CFD calculations were in good agreement with the measurements of the vane surface Mach number, film cooling row discharge

coefficients, wall heat flux and adiabatic film cooling effectiveness. Heidmann et al. [4] developed a conjugate heat transfer solver, which did not require mesh in the solid regions. This code was applied to the heat transfer analyses of the middle-span section of a film-cooled turbine vane for several materials. It was found that the conjugate heat transfer for a film-cooled vane was complicated, and the 1-D analysis between the vane surface and the plenum surface was not suitable.

However, the detailed numerical analysis of air-cooled nozzle guide vanes and shrouds with high-fidelity geometry and well-defined boundary conditions is rare. There are several reasons for this. First, the geometry of real-world turbine NGV/ shrouds is complex, particularly for internal cooling flow passages. Second, a fine mesh is needed near NGV walls to calculate properly the heat transfer [5], and thus the mesh size will be large even for a single NGV/shroud assembly. Third, it is difficult to obtain reliable boundary conditions, when both the engine combustor flow field and secondary air cooling flow are involved. The important effect of secondary air-cooling flow on the end walls of an air-film-cooled NGV was pointed out by Charbonnier et al. [6]. Fourth, perhaps the most important reason, the combustor and NGVs are directly connected, and their flow fields are closely coupled. To investigate the NGV failure adequately, the combined combustor-NGV simulation is preferred, particularly for engines where the temperature distribution at the combustor exit or NGV inlet is not uniform. Moreover, to calculate the NGV thermodynamic load with acceptable accuracy, a single high-fidelity NGV simulation is not suitable since the flow passing over each NGV is not the same, and thus an NGV sector simulation is required. The requirement for the combined high-fidelity combustor and NGV sector simulation possibly implies an impractical mesh size, thus the required computing power and time can be enormous [7].

In this chapter, an effective approach to predict the thermodynamic load of engine hot components is presented, and the failure analysis of one type of internally air-cooled NGVs is used as a demonstration case. The approach follows two steps. In the first step, a 60° combustor sector with simplified NGVs and thermocouples is simulated; and in the second step, NGV sectors are simulated where each NGV sector is comprised of one high-fidelity probe NGV and several dummy NGVs. The former identifies the NGV having the highest thermodynamic load and provides the inlet boundary conditions for the latter.

In the following sections, the computational domains and meshes of the combined combustor-NGVs and NGV sectors, numerical methods, engine operating conditions, boundary conditions, and results at flight conditions are presented and discussed. Finally, the chapter provides conclusions and recommendations going forward.

2. High-fidelity CFD models

### 2.1 Computational domain and mesh of combined combustor-NGVs

The computational domain and mesh, including a 60° sector of a traditional can-annular gas turbine combustor and simplified 10 NGVs and 3 thermocouples, is shown in **Figure 1**. The whole mesh is shown in **Figure 1(a)**; the close-up view of 10 NGVs, 3 thermocouples, and 10 NGV cooling air supply slots at the end of the annular chamber is presented in **Figure 1(b)**; and the high-fidelity combustion can mesh is illustrated in **Figure 1(c)**. In **Figure 1(c)**, the meshed components include the fuel injector, dome swirler, wiggle strips, baffle and baffle splashing holes (underneath baffles), and primary and secondary dilution holes. The external surfaces of the simplified NGVs were meshed, and the NGV internal cooling flow passages and solid metal regions were not meshed in this step. To comprise the cooling effect, the
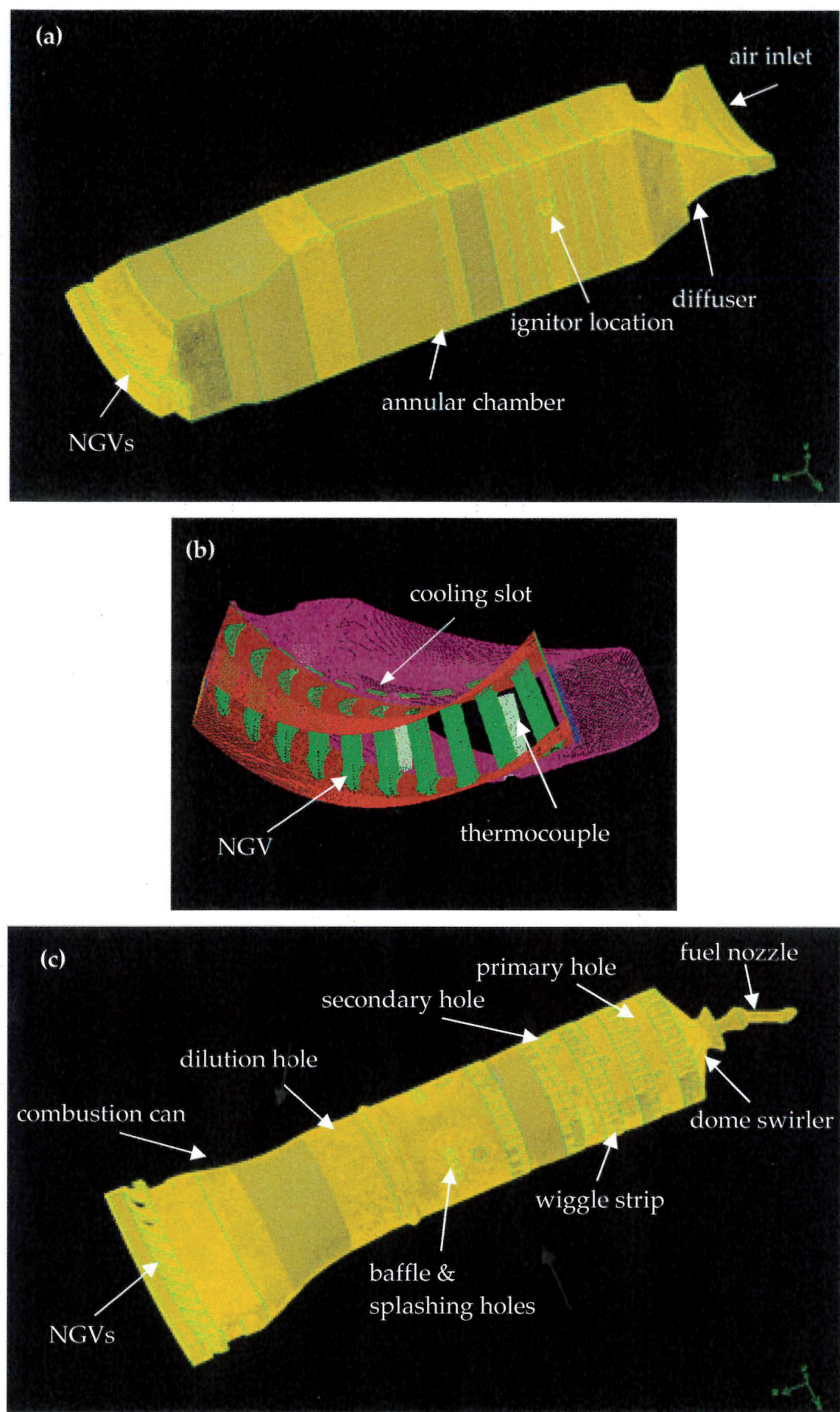
Figure 1.
Computational domain and mesh of the combined combustor-NGVs: (a) the whole mesh, (b) the NGV and thermocouple surface mesh, and (c) the can, NGVs, and thermocouple mesh.
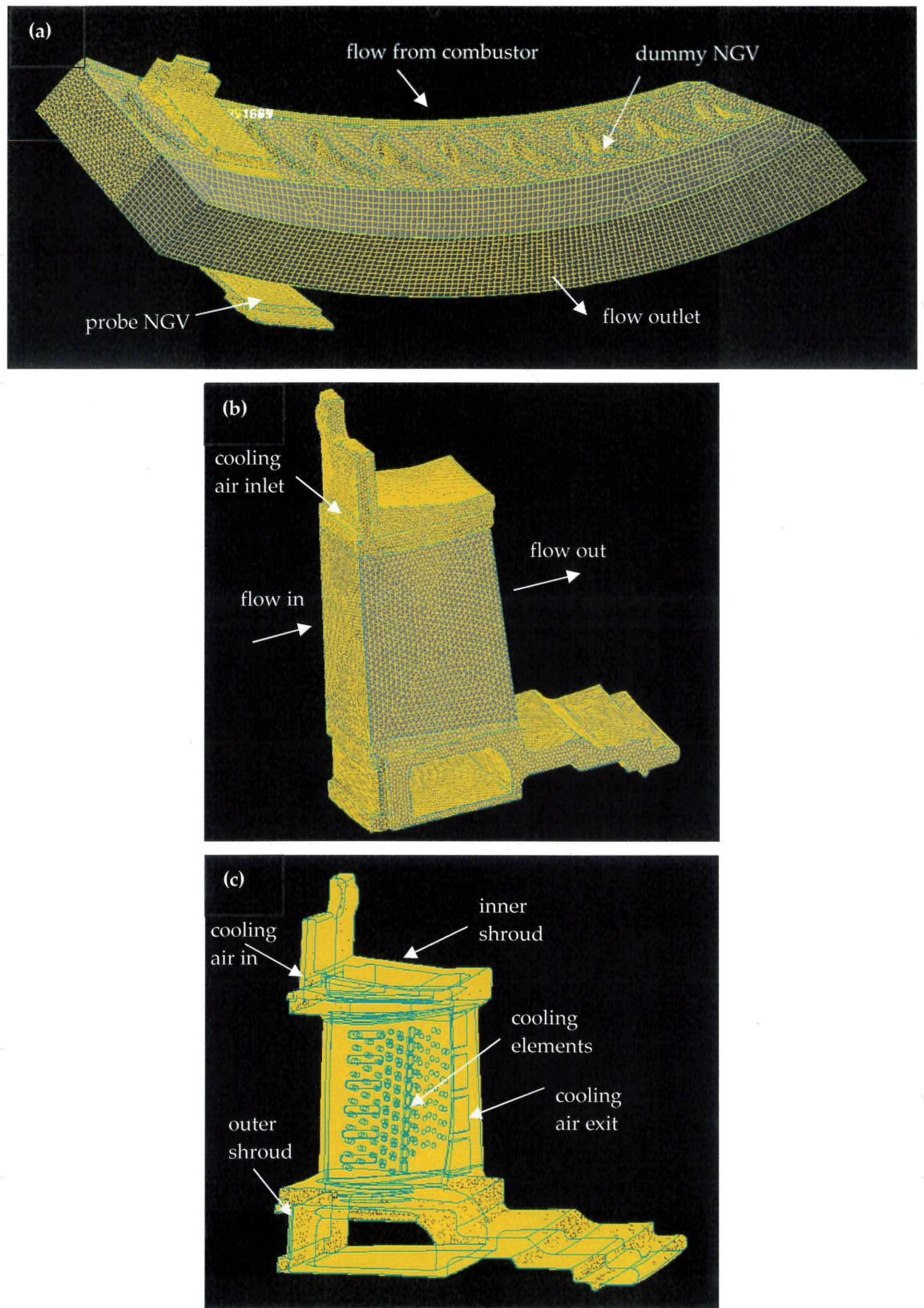
Figure 2.
NGV-2 sector domain and mesh: (a) the whole mesh, (b) the probe NGV mesh, and (c) the probe mesh in metal regions.

mean heat flux obtained from a previous single NGV simulation [8] was defined at the NGV external surfaces. More information regarding the mesh and mesh independence issue is described in Jiang and Corber [9], and the mesh size used in the simulation was 17.4 million.

As illustrated in the above figure, compressed air flows into the annular chamber throughout a narrow annulus and then flows over and enters the combustion can

through air management elements around the can or liner. In the combustion can, fine fuel droplets generated by an air-assist fuel nozzle vaporize, mix with air, and then burn, and finally the combustion products arrive at the thermocouples and NGVs.

2.2 Computational domain and mesh of NGV sector

A 60° NGV sector mesh with one high-fidelity NGV (probe NGV) and nine dummies is shown in **Figure 2(a)**, where the probe NGV is located at the second position from the left-hand side, looking upstream. The probe NGV meshes for the main portion of its domain and for regions constructed from metal are given in **Figure 2(b)** and **(c)**, respectively.

The computational domain of the NGV sector starts at the middle cross section between the NGVs and thermocouples and extends to half NGV chord length in the downstream direction. To properly solve the conjugate heat transfer, fine nodes were prescribed near the probe NGV inner and outer walls, and cooling air slot, holes and elements; and coarse nodes were generated in the regions away from the probe NGV walls. Coarse meshes were also used for the dummy NGVs. More information regarding the probe mesh and y+ value is available in [8]. A total of 7.8 million cells were used for the NGV sector simulations, and 6.6 million cells among them were for the probe NGV.

There are 10 NGVs behind the combustion can, and as seen in Section 4.1, the NGV at the second position, NGV-2, is subjected to the highest thermal load, and the NGV at the ninth position, NGV-9, experiences the lowest thermal load. For the purpose of comparison, the NGV-9 sector mesh similar to that shown in **Figure 2** was also created.

Figure 2 illustrates that the combustion gas mixture from the combustor passes through the NGV sector domain. The cooling air coming from the end of the annular chamber as shown in **Figure 1** flows into the probe NGV body at the cooling air inlet of the inner shroud, enters the internal cooling flow passages, passes through the four rectangular opens, then merges with the main flow outside the NGV, and finally runs out of the sector domain. In order to enhance the heat transfer among cooling air and NGV body, many cooling elements are constructed on either side of the cooling chamber inside the NGV though they are not clearly seen here. The cooling air absorbs heat from the NGV body through impingement and convection heat transfer and then reduces the NGV metal temperature.

3. Numerical methods

3.1 Numerical approach and physical models

For the first step, the standard Eulerian-Lagrangian method was used to solve the two-phase, steady, turbulent, compressible, reacting flows; and in the second step, steady, turbulent, compressible flows were considered [10, 11]. In both cases, the Favre-averaged governing equations for mass, momentum, species, and total enthalpy were resolved. For the coupled or conjugate heat transfer between the flow fields and solid metal regions, both fluid and metal regions were computed simultaneously. In the metal regions, since only heat conduction was concerned, the energy governing equation became simpler than that for fluid fields.

To close the flow-governing equations, the turbulence transfer terms and species and energy sources had to be properly modeled. For the combined combustor-NGV simulations, the eddy dissipation (EDS) combustion model and discrete ordinate radiation model were used to account for species and energy source terms, and the

realizable k-ε model was selected for turbulence momentum and scalar transfers. These models were carefully evaluated with the comprehensive database measured from a model combustor [12–14]. For the air-splitting over the air management elements of the combustion can, the predicted values were closely correlated to the results calculated from the semi-empirical correlations of discharge coefficients [9]. For the NGV sector simulations, the shear stress transport (SST) k-ω model was selected since it demonstrated substantial improvements in the simulations of adverse pressure gradient and separation flows in comparison with the standard k-ε and k-ω models [15]. It was successfully applied to the heat transfer simulation of a film-cooled linear cascade, in good agreement with the measured experimental results [6].

3.2 Engine operating and boundary conditions

For the combined combustor-NGV simulation, the engine takeoff conditions from reference [16] were considered in the present analysis. The air and fuel flowrates, pressure, and temperature were defined as boundary conditions at the combustor inlet for the combined combustor-NGV case. To provide the turbulent kinetic energy and dissipation rate at the air inlet, the hydraulic diameter of the inlet annulus and 5% turbulence intensity were used. At the side surfaces of the 60° sector, periodic boundaries were specified. The size and velocity components of fuel droplets in the nozzle radial direction were measured at the National Research Council of Canada's High-Pressure Spray Facility with a phase Doppler particle analyzer [9], and these data were used to define the fuel spray from the nozzle. The fuel mass flux data in the nozzle radial direction were from Rizk et al. [17]. They carried out the measurements with a mechanical patternator in a high-pressure rig at Purdue University, Indiana. Fourteen fuel spray cones (1800 droplets each) were specified, and a total of droplets in the simulation were 25,200. To consider the effect of flow tangential velocity on the pressure distribution, a radial equilibrium pressure distribution was enforced at the computational domain exit.

As mentioned earlier, the simulation results from the combined combustor-NGV simulation were used as the inlet boundary conditions for the NGV sector simulations, including the total pressure, total temperature, velocity direction, turbulence kinetic energy, and turbulence dissipation rate at the mid-cross section between the NGVs and thermocouples. To obtain the specific dissipation rate, ω, for the SST turbulence model at the inlet, the following equation was used:

$$\omega = \varepsilon / (0.09 \, k) \qquad (1)$$

where ε and k are dissipation rate and turbulence kinetic energy, respectively [18]. The NGV sector domain exit static pressure was defined from the combined combustor-NGV simulation, and it was slightly adjusted to maintain the mass flow rate. For the NGV internal cooling, 2.5% of the total inlet airflow was used. At the domain exit, the radial equilibrium pressure distribution was also enforced, and periodic boundaries were specified at the side surfaces of the 60° NGV sector. Based on the information of Mach number and flow temperature of the secondary airflow from Snedden et al. [19], the thermal boundaries on the external surfaces of shrouds were estimated, and please refer to [8] for details.

To have an overview of the NGV heat transfer processes, the Biot number of the NGV was calculated by the following equation:

$$Bi = \frac{L_c h}{k} \qquad (2)$$

where h is the mean heat transfer coefficient over the NGV airfoil external surface, L_c is the NGV airfoil characteristic length, defined as the volume divided by

the surface area, and *k* stands for the thermal conductivity of the airfoil body. The NGV is made of the X-40 alloy [20] with the density of 8610 kg/m^3, specific heat of 411 J/kg-K thermal, and conductivity of 22.8 W/m-K evaluated at 900 K. The Biot number for the NGV-2 is 0.03 which is much smaller than 0.1. It implies that the heat transfer resistance of conduction in the NGV metal body is significantly less than that of convection through the NGV/flow interfaces [21].

3.3 Solution methods

ANSYS CFD Premium, a commercial code, was used in all simulations [11]. A pressure-based coupled solver with a second-order accurate scheme was used to solve the flow fields. All simulations were well converged. For velocity components and scalar items, the normalized residuals were less than 4×10^{-5}, and for turbulent variables, they were about 6×10^{-4}. The monitored flow variables stayed unchanged for the first four digits, and it indicated that the flow steady condition is reached.

4. Results and discussion

4.1 Results of combined combustor-NGV simulation

The combined combustor-NGV simulation has provided a large amount of information. The detailed flow features have been described in [9], including the major flow parameter distributions and complex vortex structures across the dome swirler, primary and secondary dilution holes, wiggle strips, baffles, and baffle splashing holes, as well as along the mid-longitudinal plane. To give an overall picture, a few flow parameter contours along the longitudinal plane are presented here. Moreover, as required for the NGV sector simulations, the flow parameter distributions at the middle cross section between NGVs and thermocouples are discussed.

The contours of normalized static temperature, Mach number, fuel mass fraction, and normalized static pressure at the combustion can mid-longitudinal section are displayed in **Figure 3**, where the temperature and pressure are normalized by their maximum values, respectively. As seen in **Figure 3(a)**, the temperature is high in the upstream region and relatively low in the downstream region. **Figure 3(b)** indicates that Mach number is low in most of the can, increases gradually in the contraction section, and quickly reaches a maximum in the NGV section. As shown in **Figure 3(c)**, the fuel, C12H23, is mainly located in the one third upstream region of the can, which implies the chemical reaction mainly occurs in this upstream region. **Figure 3(d)** reveals that the pressure remains almost constant in most of the can region and decreases quickly in the NGV section due to flow acceleration.
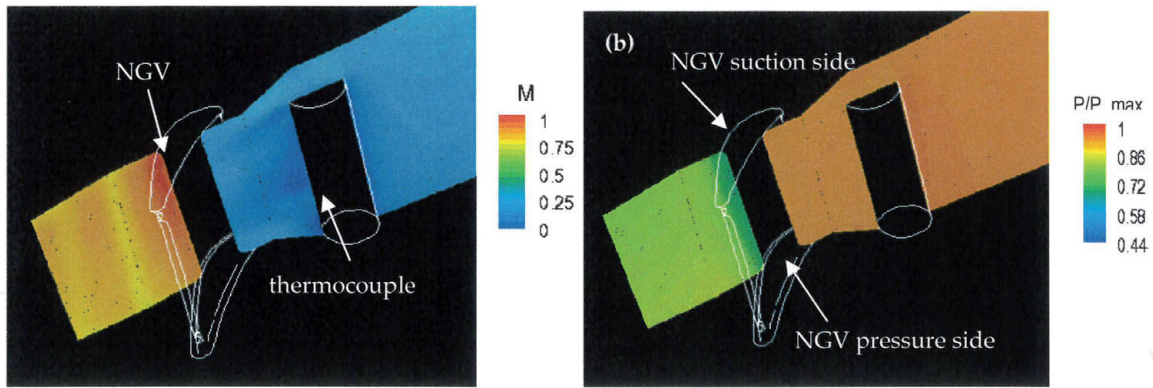
The zoomed views of **Figure 3(b)** and **(d)** near the NGV section are illustrated in **Figure 4(a)** and **(b)**, where the mid-longitudinal plane cuts through one NGV and one thermocouple. Note that the NGV and thermocouple are outlined by thin white lines. At the thermocouple stagnation point and in the wake flow region behind the thermocouple, as anticipated, the Mach number is low; and at the thermocouple stagnation point, the pressure is somewhat higher than that in the wake flow. The typical NGV flow features are observed in these two plots: the Mach number is high on the suction side and low on the pressure side; and the pressure is low on the suction side due to flow acceleration and high on the pressure side.

The contours of total temperature, total pressure, turbulent kinetic energy, and turbulence dissipation rate at the middle section between the NGVs and thermocouples are shown in **Figure 5**. In these plots the flow variables are normalized
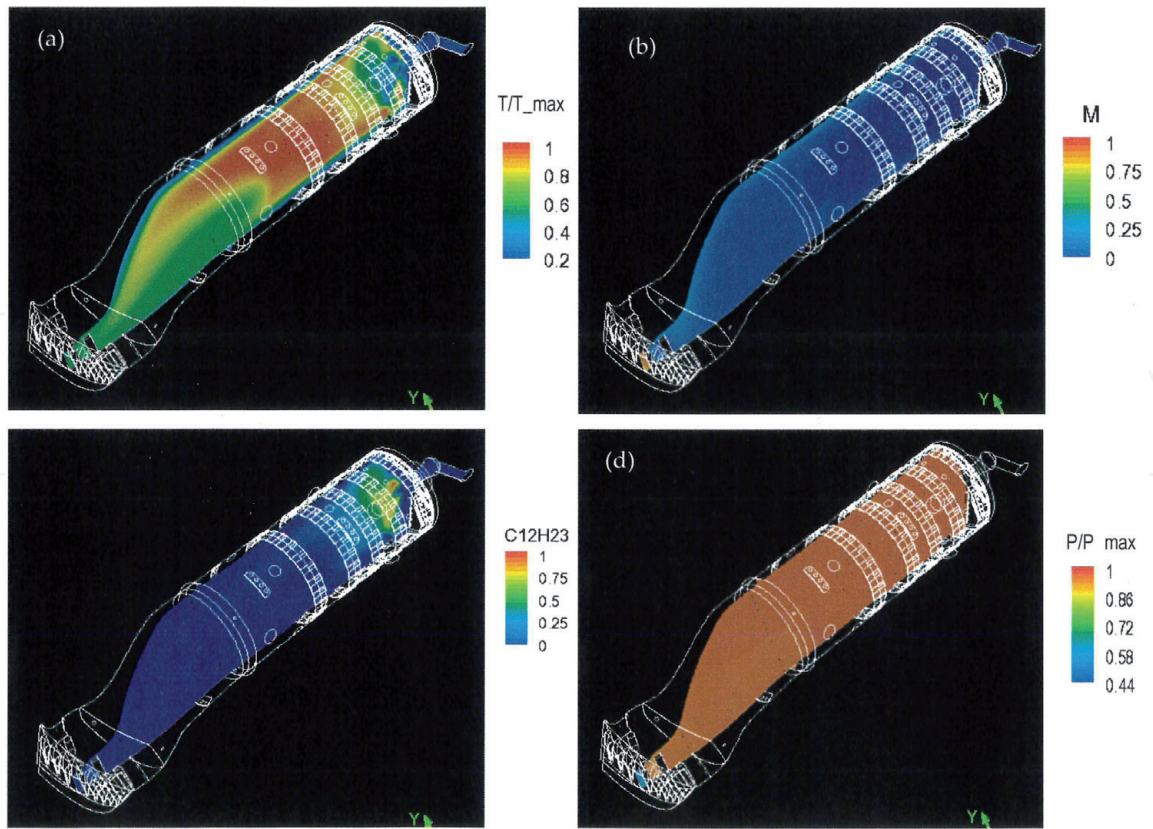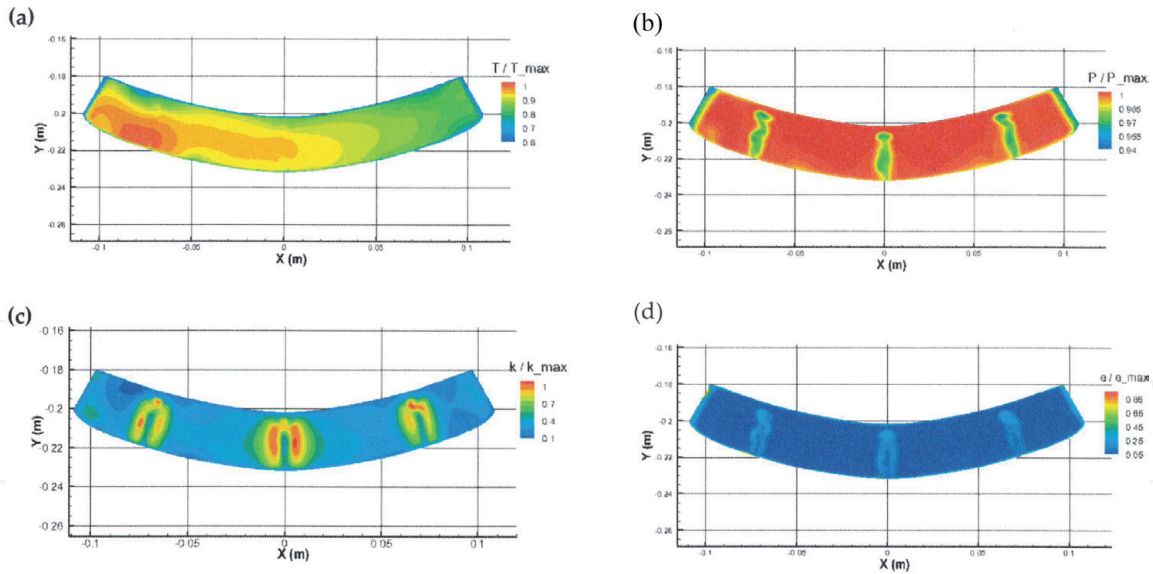
Figure 3.
Flow parameter distributions at the mid-longitudinal section: (a) normalized static temperature, (b) Mach number, (c) C12H23 mass fraction, and (d) normalized static pressure.
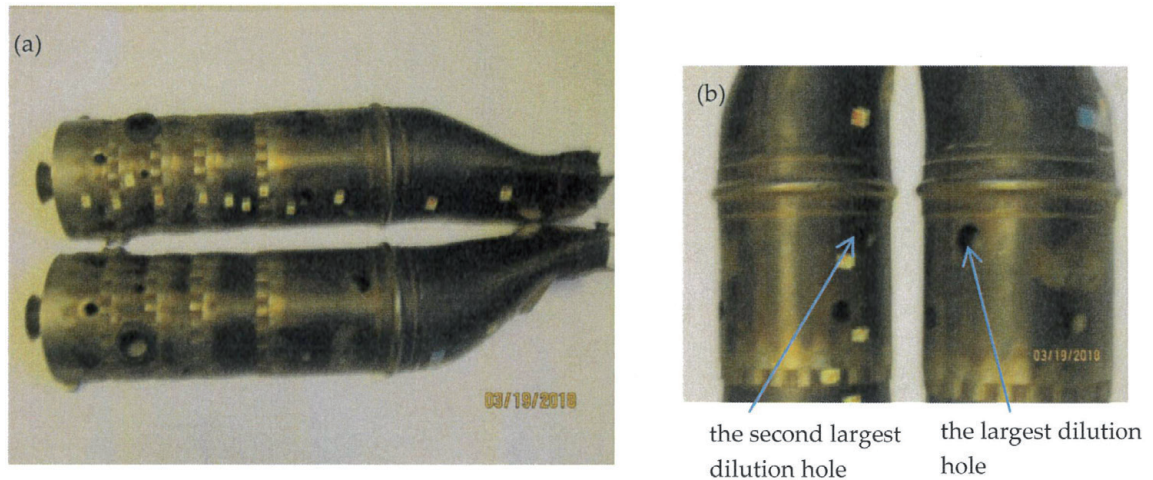

Figure 4.
*(a) The zoomed view of **Figure 3(b)** near NGV section and (b) the zoomed view of **Figure 3(d)** near the NGV section.*

by their section maximum values, respectively. **Figure 5(a)** clearly shows the hot streaks or temperature distortions from the combustor. The normalized temperature changes from 0.61 to 1.0 and has an average value of 0.888. These values are in excellent agreement with the experimental data, T_average = 0.886 and T_max = 1.0025 [17]. The deviations in the mean and maximum temperatures are less than 0.5%. This provides more confidence for the subsequent NGV failure analysis.

The cause of the hot streaks from the combustion can exit can be readily clarified by its geometry. As shown in **Figure 6**, the largest and second largest dilution holes just upstream of the contraction section are asymmetrically located with reference to the can mid-longitudinal plane, and this is the main reason of the temperature distortion at the combustor exit.

Figure 5.
Normalized flow parameter contours at the cross section between the NGVs and thermocouples: (a) the total temperature, (b) the total pressure, (c) the turbulent kinetic energy, and (d) the turbulence dissipation rate.


the second largest dilution hole

the largest dilution hole

Figure 6.
*Combustion can: (a) two halves and (b) the two dilution holes before the contraction section.*

As observed in **Figure 5(b)**, there are three narrow relatively low total pressure regions at the cross section, which are the wake flows of the three thermocouples. Moreover, the total pressure near the two-side boundaries is also low. This is mainly due to the flow passage increase in the circumferential direction to house two-side NGVs. **Figure 5(c)** and **(d)** reveals that the turbulent kinetic energy and dissipation rate are high in the wake flow regions of the thermocouples. It is interesting to note the rotating vortices in these local regions, from near the can inner wall to the can outer wall. It is believed that this phenomenon is caused by the gaps between the thermocouples and the can inner wall (please see **Figure 1(b)** or **Figure 4**). As usual, the turbulence dissipation rate near the surrounding walls is high.

Figure 7 displays the temperature distributions at the outer surfaces of the simplified 10 NGVs and at the mid-cross section between the NGVs and thermocouples. The comparison of temperature variations and mean temperatures over these NGVs indicates that among the 10 NGVs, the highest surface maximum temperature and mean temperature occur at NGV-2, while the lowest maximum and mean values happen at NGV-9. These results indicate that NGV-2 is the most vulnerable NGV under the flight condition, and this agrees with the field-observed NGV damage pattern.
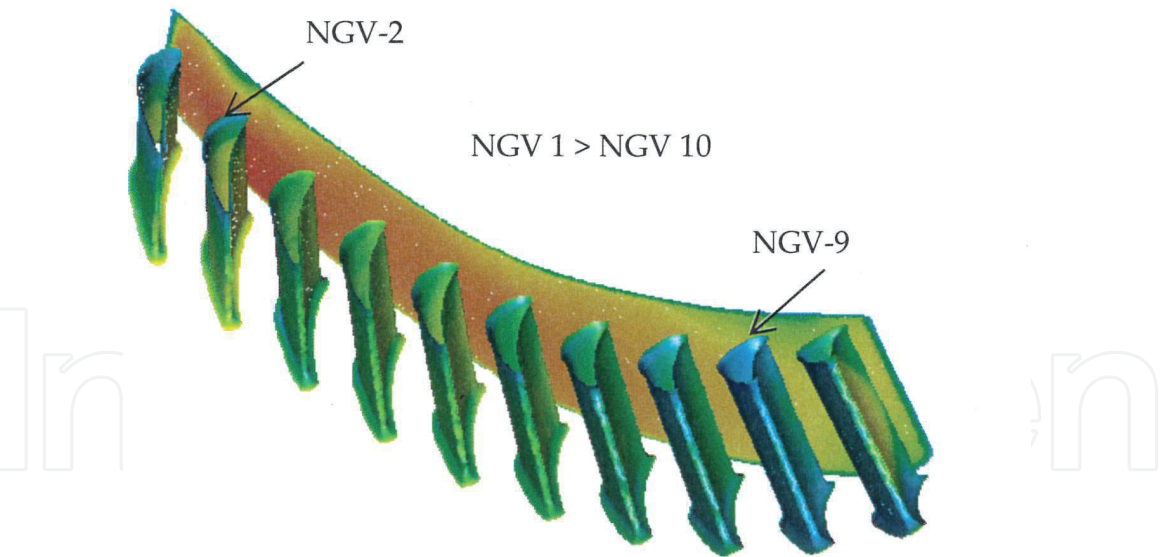
Figure 7.
Normalized static temperature contours at the external surfaces of the simplified NGVs and at the middle cross section between the NGVs and thermocouples.
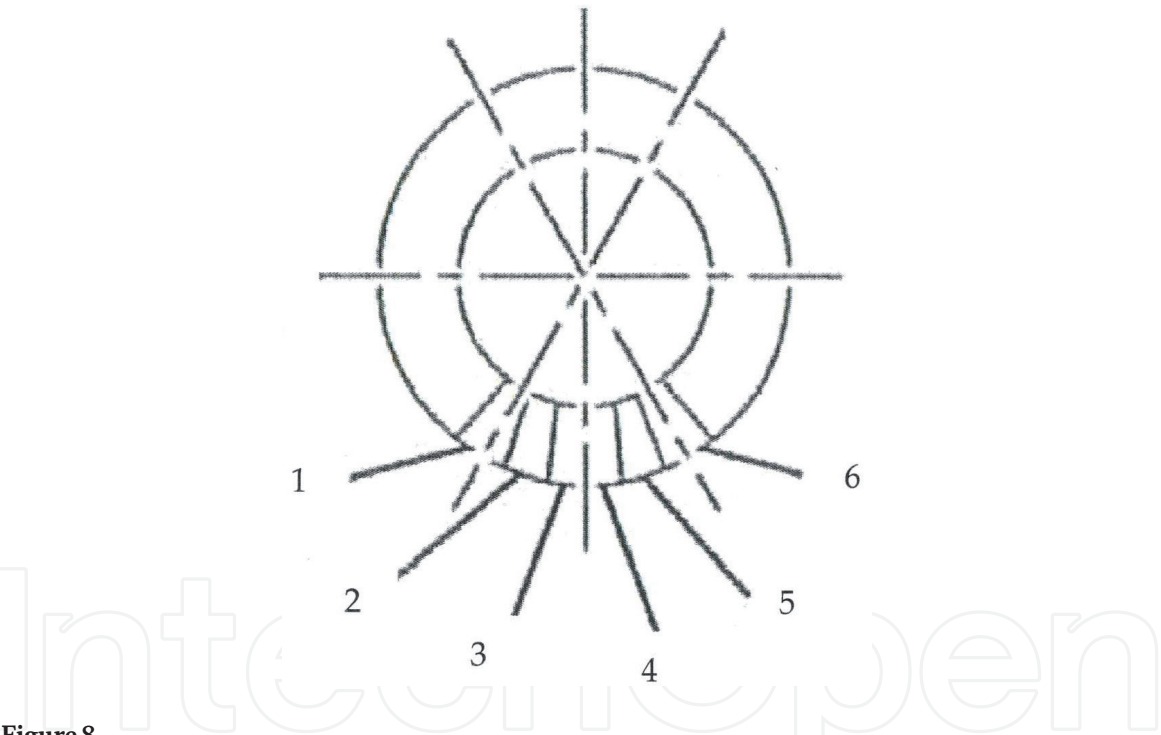
Figure 8.
The locations of six NGV units relative to the combustion can exit, looking upstream.

The locations of six NGV units relative to the combustion can exit are outlined in **Figure 8**. A 60° sector is formed by two dashed lines, and the overlapped line with the small circle defines the combustion can exit. Each NGV unit has two NGVs, and the leading NGV and trailing NGV are named counterclockwise, looking upstream. **Figure 8** indicates that the trailing NGV of Unit 1 and the leading NGV of Unit 6 are within the can exit domain. Thus there are 10 NGVs behind each combustion can. Most of the failures are Unit 2, while a few are Unit 1 or Unit 6, the clockwise neighbors of Unit 2.

4.2 Results of NGV sector simulations

A large amount of data was obtained from the NGV sector simulations at the flight conditions. The main features of the complex flow field and heat transfer have

been previously described in [8]. Here the results related to the NGV failure analysis are presented and discussed.

Shown in **Figures 9** and **10** are the external surface temperatures of the NGV/shrouds for the three cases: NGV-2, NGV-2 with the averaged inlet flow parameters, and NGV-9, where the temperatures are normalized by the same maximum values.

Figures 9–11 clearly reveal that the thermal load of NGV-2 is highest among the three cases. Its maximum surface normalized temperature reaches 0.96, 6.8% higher than NGV-2 with the mean inlet conditions, and 10.7% higher than NGV-9. The mean surface temperature of NGV-2 is 0.80, 2.5% higher than the second case and 5.7% higher than the third case. These results confirm the strong hot streak effect on the NGV thermal load, where a large increase in the metal temperature can result in significant decrease in strength [22]. Some means of thermal protection, such as the addition of thermal barrier coating (TBC) and/or improvement of the internal cooling arrangement, should be considered for the vulnerable NGVs.

Of greater significance in **Figures 9–11** is that for all three cases, there is a nearly circular high-temperature zone in the middle of the NGV pressure side, shifted slightly towards the leading edge and outer shroud. In contrast, on the suction side, there is no high-temperature zone observed in the middle, and the temperature variation is less than for the pressure side. Note that for the second case, the hot streak effect is not included since the averaged inlet boundary conditions are used. These observations clearly explain the root cause of the mid-span cracking of the NGVs,
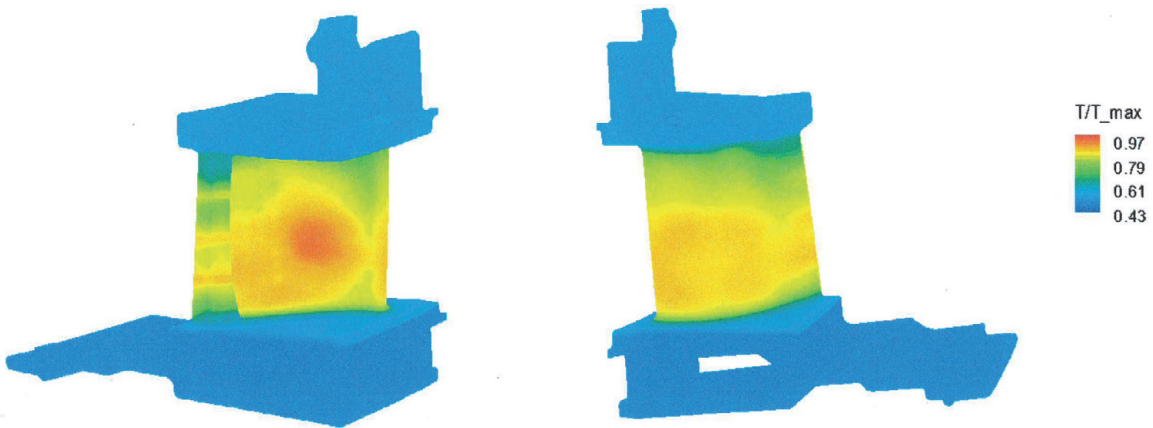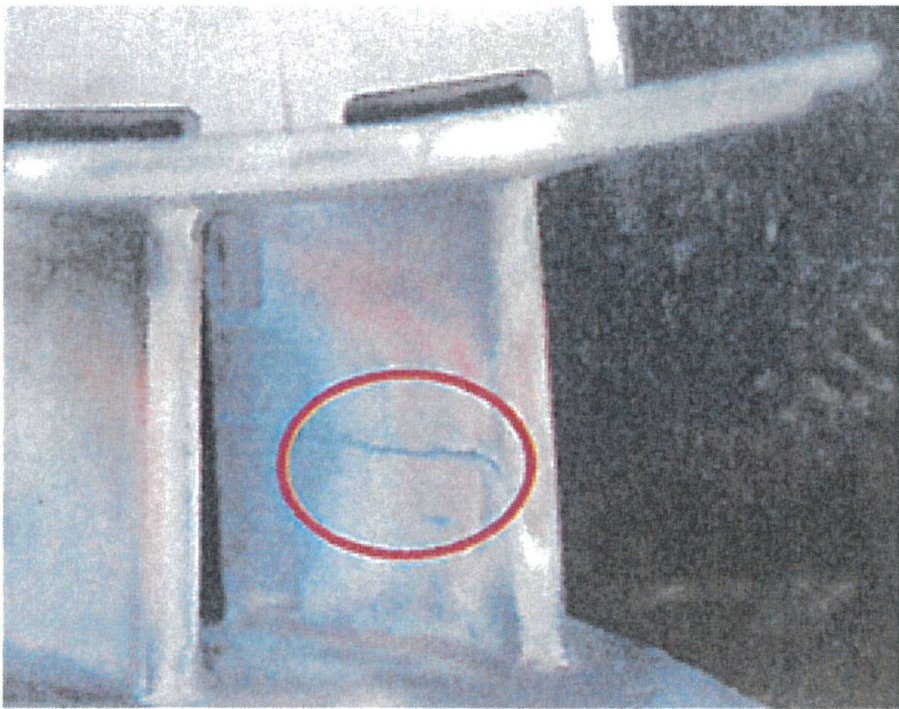

Figure 9.
Normalized temperature contours at the external surfaces of the NGV/shrouds for the probe NGV at the second position, NGV-2.
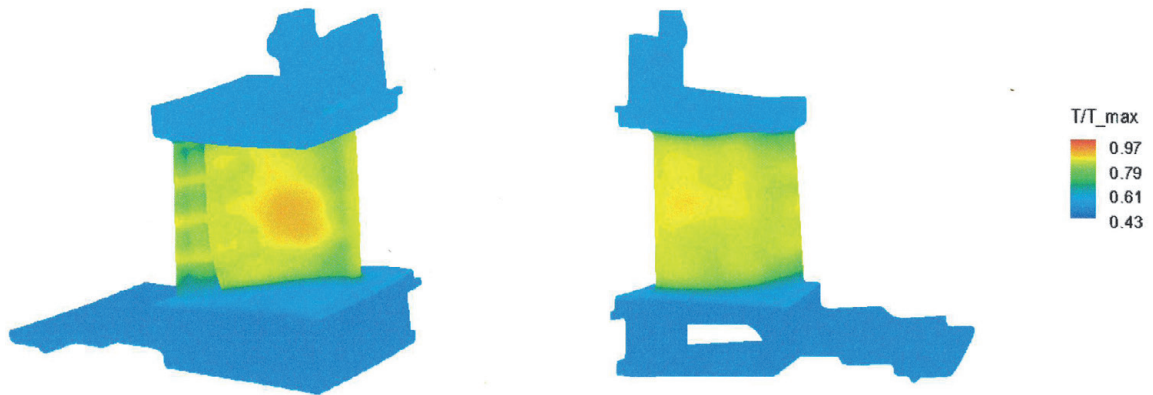
Figure 10.
Normalized temperature contours at the external surfaces of the NGV/shrouds for the probe NGV at the second position, NGV-2, with the averaged inlet flow conditions.
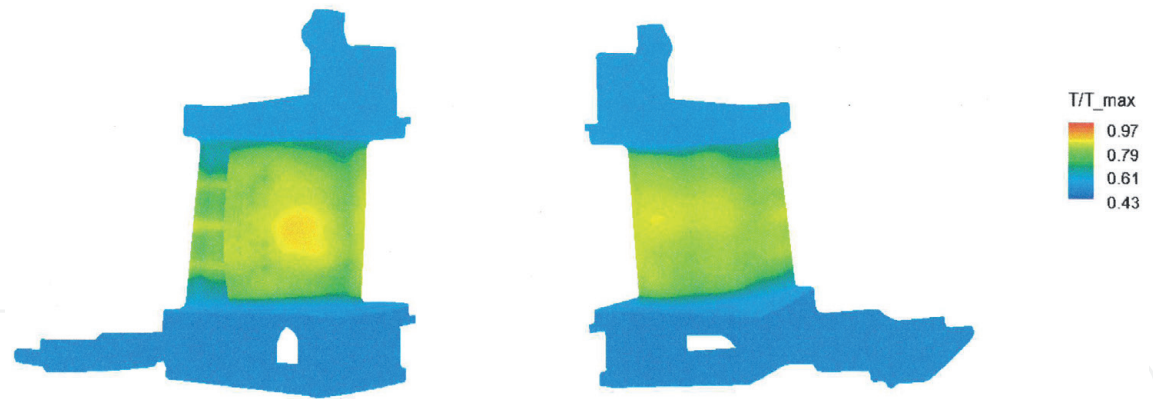
Figure 11.
Normalized temperature contours at the external surfaces of the NGV/shrouds for the probe NGV at the ninth position, NGV-9.
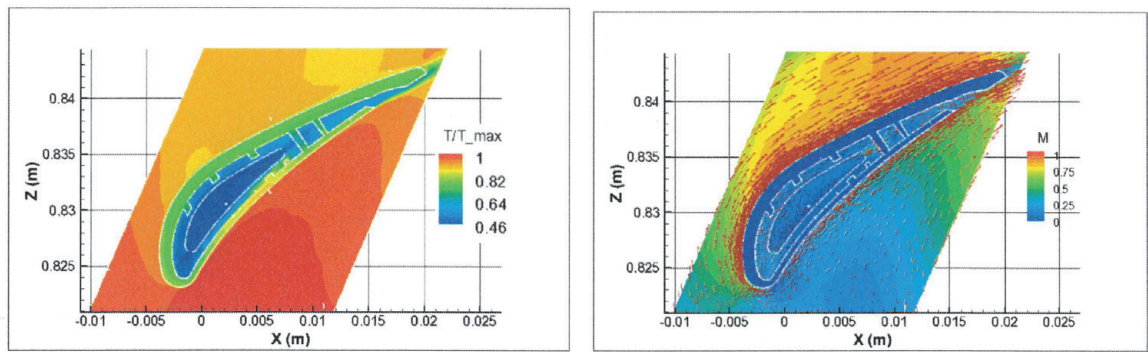

Figure 12.
*Typical mid-span cracking on the pressure sides.*

which are consistent with the field-observed NGV damages as shown in **Figure 12**. As shown in in Figure 12, the crack is at the mid-span of the NGV pressure side.

For the above three cases, **Figures 13–15** present the distributions of static temperature, Mach number, and velocity vectors at the section across the 5th trailing-edge hole and the 11th leading-edge cooling hole counted from the cooling air inlet. The maximum incoming flow temperature is used to normalize temperature contour plots. The maximum incoming temperature is 1.0 for the first case, 0.91 for the second, and 0.87 for the third. The incoming temperature difference between NGV-2 and NGV-9 is 0.13, which results in the considerable difference in their thermal loads. The typical NGV flow features are illustrated in these figures. The temperature is high at the pressure side and gradually decreases along the suction side; and the Mach number is low near the leading edge, gradually increases along the pressure side and increases and then decreases along the suction side. The velocity vectors from the leading-edge cooling hole illustrate the impingement cooling, and the velocity vectors along the internal and external walls represent the convection cooling.
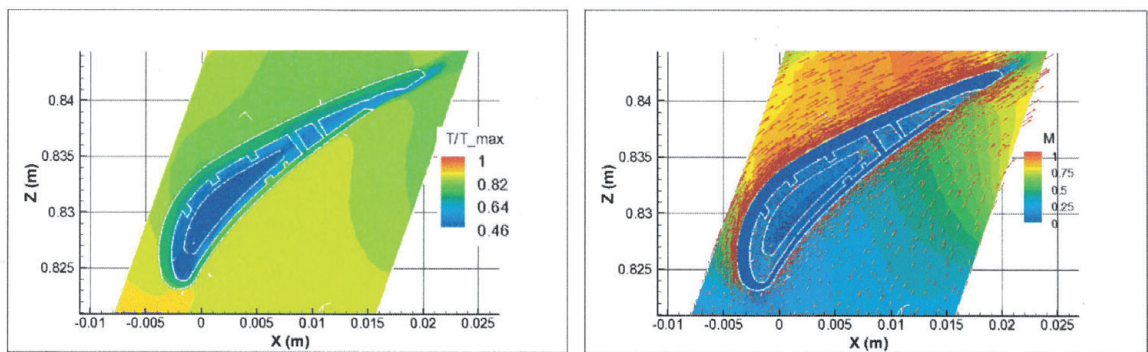
Figure 13.
Normalized temperature and Mach number contours and velocity vectors at the section across one trailing-edge cooling hole and one leading-edge cooling hole for the pin-fin NGV-2.
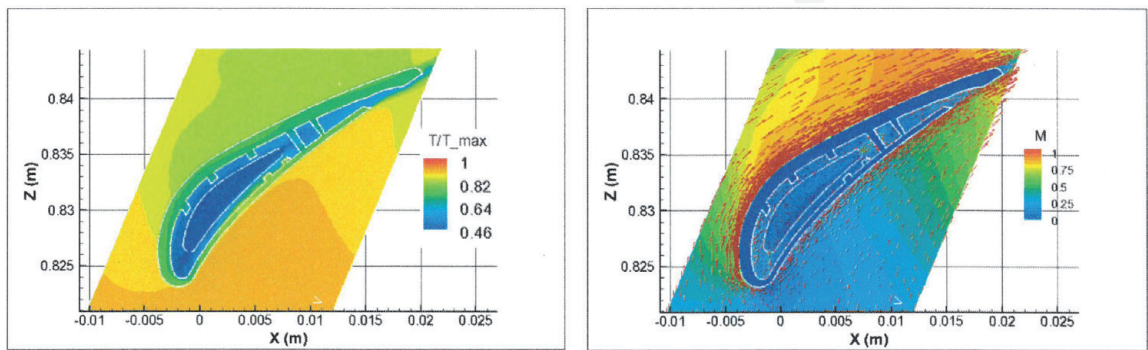
Figure 14.
Normalized temperature and Mach number contours and velocity vectors at the section across one trailing-edge cooling hole and one leading-edge cooling hole for the pin-fin NGV-2 with the averaged inlet flow parameters.

Figure 15.
Temperature and Mach number contours and velocity vectors at the section across one trailing-edge cooling hole and one leading-edge cooling hole for the pin-fin NGV-9.

5. Conclusions

In this chapter, the flow fields and heat transfer of the combined combustor-NGV simulation and the NGV sector simulations have been successfully simulated. The predicted temperature distribution at the combustor exit is in excellent agreement with the experimental data, which provides more confidence in the NGV failure analysis.

The results of the first step analysis indicate that NGV-2 has the highest thermal load and NGV-9 has the lowest thermal load at the flight conditions, which is consistent with the NGV damage pattern. Therefore, it is concluded that the field-observed NGV damage pattern is caused by the hot streaks from the combustor, and this provides a good foundation for the second step analysis.

In the second step analysis, it is found that there is a circular high-temperature zone in the middle of the NGV on the pressure side, shifted slightly towards the leading edge and outer shroud for all cases studied, which is consistent with the location where the mid-span cracking occurs. Consequently, it is concluded that the root cause of the NGV mid-span cracking is the high thermal loading, or stated another way, an inadequate cooling arrangement.

In summary, the CFD analysis has successfully identified not only the root cause of the NGV failure pattern but also the root cause of the NGV failure location. This excellent example demonstrates the effectiveness of the two-step and dummy component approach to investigate turbine hot component failures, and its advantages are as follows:

1. With the dummy component approach, the computing time is greatly reduced. In this example, with nine dummy NGVs, the computing time of the NGV sector simulation is reduced to about one tenth of that without the dummy component approach.

2. The separation of high-fidelity combustor and high-fidelity component sector simulations makes it more practical to obtain the reliable inlet boundary conditions for component sector simulations with accepted computing time.

3. This approach is more suitable to the workplace where the computing power and memory size are limited.

Acknowledgements

Author details

Lei-Yong Jiang* and Prakash Patnaik
Aerospace Research Centre, National Research Council of Canada, Ottawa, Ontario, Canada

*Address all correspondence to: lei-yong.jiang@nrc-cnrc.gc.ca

IntechOpen

References

[1] Saravanamuttoo HIH, Rgers CFC, Cohen H. Gas Turbine Theory. 5th ed. UK: Pearson Education Limited; 2001

[2] Mazur Z, Hernandez-Rossette A, Garcia-Illescas R, Luna-Ramirez A. Analysis of conjugate heat transfer of a gas turbine first stage nozzle. Applied Thermal Engineering. 2006;**26**:1796-1806

[3] Harsqama SP, Burton CD, Chana KS. Measurements and computations of external heat transfer and film cooing in turbines. In: The Proceedings of the 10th International Symposium on Air Breathe Engines (ISABE); 1991. pp. 1276-1284

[4] Heidmann JD, Kassab AJ, Divo EA, Franklin Rodriguez F, Steinthorsson E. Conjugate Heat Transfer Effects on a Realistic Film-cooled Turbine Vane, ASME IGTI paper, GT2003-38553; 2003

[5] Jiang LY, Manipurath S, Bourque G, Houde M. Flow-field of a triple-walled gas-sampling probe with sub-cooled boiling effect. Flow Measurement and Instrumentation. 2007;**18**:156-116

[6] Charbonnier D, Ott P, Jonsson M, Kobke Th, Cottier F. Comparison of Numerical Investigations with Measured Heat Transfer Performance of a Film Cooled Turbine Vane, ASME IGTI paper, GT2008-50623; 2008

[7] Mongia HC. Recent Advances in the Development of Combustor Design Tools, AIAA Paper 2003-4495; 2003

[8] Jiang LY, Wu X, Zhong Zhang Z. Conjugate heat transfer of an internally air-cooled nozzle guide vane and shrouds. Advances in Mechanical Engineering. 2014;**2014**:146523. DOI: 10.1155/2014/146523

[9] Jiang LY, Corber PA. Air Distribution over a Combustor Liner, IGTI paper, GT-2014-25405; 2014

[10] Stiesch G. Modelling Engine Spray and Combustion Processes. New York: Springer; 2003

[11] ANSYS Fluent Inc. Fluent 19 documentation, 10 Cavendish Court, Lebanon, NH 03766, USA; 2018

[12] Jiang LY, Campbell I. Radiation benchmarking in a model combustor. Journal of Engineering for Gas Turbines and Power. 2009;**131**:011501

[13] Jiang LY, Campbell I. Application of three combustion models to a model combustor. Canadian Aeronautics and Space Journal. 2005;**51**(1):1-11

[14] Jiang, L.Y., Chapter 7: RANS modelling of turbulence in combustors, in The Book of Turbulence Modelling Approaches—Current State, Development Prospects, Applications, Edited by Dr. Konstantin V., IntechOpen, ISBN: 978-953-51-5311-5, 2017

[15] Menter FR. Two-equation Eddy-viscosity turbulence models for engineering applications. AIAA Journal. 1994;**32**(8):1598-1605

[16] Oechsle VL, Ross PT, Mongia HC. High Density Fuel Effects on Gas Turbine Engines, AIAA-87-1829; 1987

[17] Rizk NK, Oechsle VL, Ross PT, Mongia HC. High Density Fuel Effects, Technical Report AFWAL-TR-88-2046, Wright-Patterson Air Force Base, Aero Propulsion Laboratory, USA; 1988

[18] Wilcox DC. Turbulence Modelling for CFD. second ed. La Canada, California, USA: DCW Industries Inc.; 2002

[19] Snedden G, Roos T, Naidoo K. Detailed Disc Assembly Temperature Prediction: Comparison between CFD and Simplified Engineering Methods, ISABE paper 2005-1130; 2005

[20] Brown WF Jr, Setlak SJ. Aerospace
Structural Materials Handbook. 38th ed.
Purdue University: CINDA/USAF CRDA
Handbooks Operation; 2004

[21] Incropera FP, DeWitt DP.
Fundamentals of Heat and Mass
Transfer. fifth ed. USA: John Wiley and
Sons, Inc.; 2002

[22] Klopp WD. Non-Ferrous Alloys,
Co. MAR-M-509, Aerospace Structural
Metals Handbook; 1985